AFRL-RW-EG-TR-2018-095

Bounding Visual Odometry Drift with Radio Range Data for Small Unmanned Aerial Vehicles

Robert C Leishman, Jeremy Gray, John Raquet,[1] Adam Rutkowski,[2] Wil Myrick[3]

Department of the Air Force
Air Force Material Command AFRL—
Eglin Research Site Munitions
Directorate
101 West Eglin Blvd
Eglin AFB FL, 32542-6864

April 2018

Final Report

Period of Performance: October 2013–October 2017

AIR FORCE RESEARCH LABORATORY MUNITIONS DIRECTORATE
EGLIN AIR FORCE BASE - AIR FORCE MATERIEL COMMAND - UNITED STATES AIR FORCE

NOTICE AND SIGNATURE PAGE

REPORT DOES NOT CONTAIN SBIR DATA RIGHTS INFORMATION

Using Government drawings, specifications, or other data included in this document for any purpose other than Government procurement does not in any way obligate the U.S. Government. The fact that the Government formulated or supplied the drawings, specifications, or other data does not license the holder or any other person or corporation; or convey any rights or permission to manufacture, use, or sell any patented invention that may relate to them.

In House report

Qualified requestors may obtain copies of this report from the Defense Technical Information Center (DTIC) <http://www.dtic.mil/dtic/index.html>.

AFRL-RW-EG-TR-2018-095 HAS BEEN REVIEWED AND IS APPROVED FOR PUBLICATION IN ACCORDANCE WITH ASSIGNED DISTRIBUTION STATEMENT.

FOR THE DIRECTOR:

//SIGNED//

ADAM J. RUTKOWSKI, DR-III, DAF
Work Unit Manager
Autonomy, Navigation and
Control Branch

Digitally signed by DOUCETTE.EMILY.A.1298118382
Date: 2023.11.28 12:23:35 -06'00'

EMILY A. DOUCETTE, DR-III, DAF
Science & Technical Advisor,
Autonomy, Navigation and
Control Branch

This report is published in the interest of scientific and technical information exchange, and its publication does not constitute the Government's approval or disapproval of its ideas or findings.

REPORT DOCUMENTATION PAGE

Form Approved
OMB No. 0704-0188

1. REPORT DATE *(DD-MM-YYYY)*	**2. REPORT TYPE**	**3. DATES COVERED** ***(From–To)***
21-04-2018	Final	23-10-2013–23-10-2017

4. TITLE AND SUBTITLE

Bounding Visual Odometry Drift with Radio Range Data for Small Unmanned Aerial Vehicles

5a. CONTRACT NUMBER
N/A

5b. GRANT NUMBER
N/A

5c. PROGRAM ELEMENT NUMBER
N/A

6. AUTHOR(S)

Robert C Leishman, Jeremy Gray, John Raquet, Adam Rutkowski, Wil Myrick

5d. PROJECT NUMBER
N/A

5e. TASK NUMBER
N/A

5f. WORK UNIT NUMBER
W0QC

7. PERFORMING ORGANIZATION NAME(S) AND ADDRESS(ES)

Department of the Air Force
Air Force Material Command
AFRL—Eglin Research Site
Munitions Directorate
101 West Eglin Blvd
Eglin AFB FL, 32542-6864

8. PERFORMING ORGANIZATION REPORT NUMBER
N/A

9. SPONSORING/MONITORING AGENCY NAME(S) AND ADDRESS(ES)

Department of the Air Force
Air Force Material Command
AFRL—Eglin Research Site
Munitions Directorate
101 West Eglin Blvd
Eglin AFB FL, 32542-6864

10. SPONSOR/MONITOR'S ACRONYM(S)
AFRL/RWTA

11. SPONSOR/MONITOR'S REPORT NUMBER(S)
AFRL-RW-EG-TR-2018-095

12. DISTRIBUTION/AVAILABILITY STATEMENT

DISTRIBUTION STATEMENT A —Approved for public release: distribution unlimited. AFRL-2024-0362

13.SUPPLEMENTARY NOTES

Distribution Statement indicating authorized access is on the cover page and block 12 of this form. Data rights restrictions and availability of this report are shown on the Notice and Signature page. Report contains color.

14. ABSTRACT

Vision-aided navigation for unmanned aerial vehicles (UAVs) is a well-researched topic. Global Navigation Satellite System (GNSS) information is valuable and used on a routine basis, however having multiple methods of obtaining navigation information for small UAVs is desirable. One popular method of utilizing vision information for UAV navigation is that of Visual Odometry (VO), even though without additional aides, position drift is unbounded for this approach. This study investigates the amount of additional information that is required to bound the position drift for a UAV that is using a VO algorithm at the heart of its navigation solution. The proposed method is to utilize a pair of ranging radios between a GNSS denied UAV navigating with VO and another UAV that has access to good GNSS information, giving it a known location. A flight test recreating this scenario was performed in July 2017 and the data are used to demonstrate the proposed concept. In addition to test data, an analytic observability analysis is presented.

15. SUBJECT TERMS

tightly coupled global positioning system, tightly coupled GPS, vision-aided inertial navigation, zero velocity update

16. SECURITY CLASSIFICATION OF:			**17. LIMITATION OF ABSTRACT**	**18. NUMBER OF PAGES**	**19a. NAME OF RESPONSIBLE PERSON**
					ADAM RUTKOWSKI
a. REPORT	**b. ABSTRACT**	**c. THIS PAGE**	UNCLASSIFIED	31	**19b. TELEPHONE NUMBER** ***with area code***
UNCLASSIFIED	UNCLASSIFIED	UNCLASSIFIED			850-883-2632

Standard Form 298 (Rev. 8-98)
Prescribed by ANSI Std. Z39.18

THIS PAGE INTENTIONALLY LEFT BLANK

TABLE OF CONTENTS

LIST OF FIGURES

Figure **Page**

1 SUMMARY

Vision-aided navigation for unmanned aerial vehicles (UAVs) is a well-researched topic. Global Navigation Satellite System (GNSS) information is valuable and used on a routine basis, however having multiple methods of obtaining navigation information for small UAVs is desirable. One popular method of utilizing vision information for UAV navigation is that of Visual Odometry (VO), even though without additional aides, position drift is unbounded for this approach. This study investigates the amount of additional information that is required to bound the position drift for a UAV that is using a VO algorithm at the heart of its navigation solution. The proposed method is to utilize a pair of ranging radios between a GNSS denied UAV navigating with VO and another UAV that has access to good GNSS information, giving it a known location. A flight test recreating this scenario was performed in July 2017 and the data are used to demonstrate the proposed concept. In addition to test data, an analytic observability analysis is presented.

2 INTRODUCTION

Vision-aided navigation for unmanned aerial vehicles (UAVs) is a well-researched topic. Global Navigation Satellite System (GNSS) information is valuable and used on a routine basis, however having multiple methods of obtaining navigation information for small UAVs is desirable in the event that, for whatever reason, accurate and reliable GNSS information is unavailable. Recent examples of vision-based UAV navigation include [1], [2], [3], [4], [5], [6], [7], [8], [9].

One popular method of utilizing vision information for UAV navigation is that of Visual Odometry (VO). VO is the process of extracting incremental motion information out of successive camera images. Excellent tutorials on the subject, explaining the major methodologies and approaches of VO, are available in [10], [11]. The difficulty with using VO information is that the transformation is relative to the camera frame and not relative to an earth-fixed navigation frame, causing an unbounded position solution. With a pure VO approach and no loop closure constraints, the position error will grow without bound.

The study documented in this paper investigates the amount of additional information that is required to bound the position drift for a UAV that is using a VO algorithm at the heart of its navigation solution. The proposed method is to utilize a pair of ranging radios between the GNSS denied UAV navigating with VO and another UAV that has a good GNSS location solution. The idea is that the UAV with access to GNSS information is able to fly higher, above the range of jamming, out of the urban canyon, or out of whatever condition that is limiting the access to GNSS signals to the lower plane. Meanwhile, the lower UAV navigates primarily using VO information but can receive the range to and position of the higher UAV.

A flight test recreating this scenario was conducted in July 2017 and the data are used to demonstrate the proposed concept. The research here builds on initial work in [12]. All the results are focused on estimating the position of the lower UAV.

The paper is organize as follows: first we derive the filter representation, the vehicle state and the measurement updates in Section 3. Next in Section 4 we examine an analytical observability analysis to show that the proposed ranging system can bound the drift.

Section 5 provides details regarding the flight test and hardware resources. The results of the flight test demonstrating a bounding of drift are in Section 6. Conclusions are provided at the end of the paper.

3 FILTER REPRESENTATION

We first introduce the coordinate frames utilized throughout the paper in preparation of the filter derivation, illustrated in Figure 1. The first coordinate frame is the body-fixed frame of the lower UAV, which is fixed to the center of mass of the vehicle with the $\hat{\imath}_b$ axis out the nose, the $j\hat{b}$ axis out the right wing, and $\hat{k}_b$ axis out of the belly. The second is the navigation frame, which is a local frame with the $\hat{\imath}_N$ axis aligned with magnetic North, the $j\hat{N}$ axis aligned with East, and the $\hat{k}_N$ axis pointing toward the center of the Earth [13]. The navigation frame sits at a point on the Earth's surface near where the flight occurs and for short, low altitude UAV flights is assumed to be inertial [14]. We utilize the convention described in [14], Chapter 2, including the 3-2-1 Euler angle sequence and the wind triangle.

The extended Kalman filter used to demonstrate bounding of a Visual Inertial Odometry (VIO) solution, which fuses IMU, pressure, VO and range measurements, largely follows the development in Chapter 8 of [14]. We have extended the filter by including states for altitude and vertical velocity. The states for the filter are the north position, east position, ground speed, course angle, wind speed in north direction, wind speed in east direction, yaw, altitude, and vertical velocity:

$$x = [p_n \, p_e \, V_g \, \chi \, \omega_n \, \omega_e \, \psi \, p_a \, \dot{p}_a]^T \tag{1}$$

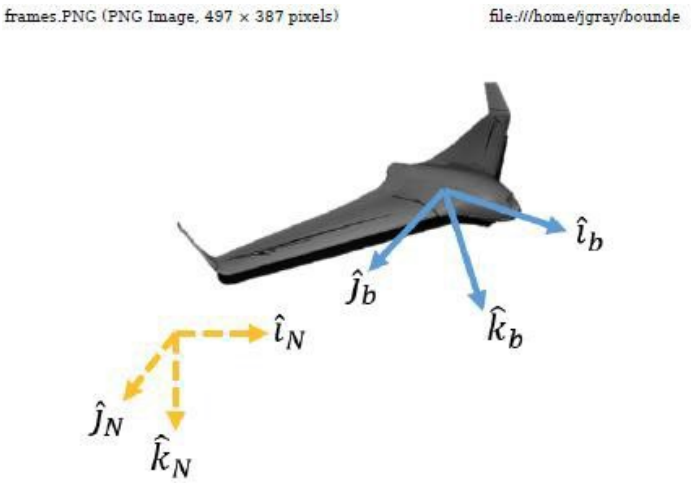

Figure 1. Coordinate frames used in the filtering derivations. Body-fixed frame is in blue, the inertial frame is in orange.

The north, east and altitude positions are with respect to the navigation frame. Altitude is simply the negative of the position in the down direction. The relationship between ψ and χ is explained using the wind triangle [14]. ψ is the angle between the $\hat{\imath}_N$ axis and the $\hat{\imath}_b$ axis in the horizontal plane. χ is the angle between the $\hat{\imath}_b$ axis and the ground speed vector, in the horizontal plane.

The state x advances according to the nonlinear model $\dot{x} = f(x, u)$, where the input u is composed of the airspeed, pitch rate, yaw rate, roll angle, pitch angle:

$$u = [V_a \; q \; r \; \phi \; \theta]^T \tag{2}$$

$$f(x,u) = \begin{bmatrix} V_g \cos(\chi) \\ V_g \sin(\chi) \\ \frac{(V_a \cos(\psi)+\omega_n)(-V_a\dot{\psi} \sin(\psi))+(V_a \sin(\psi)+\omega_e)(V_a\dot{\psi} \cos(\psi))}{V_g} \\ \frac{g}{V_g}\tan(\phi)\cos(\chi-\psi) \\ 0 \\ 0 \\ q\frac{\sin(\phi)}{\cos(\theta)}+r\frac{\cos(\phi)}{\cos(\theta)} \\ \dot{p}_a \\ 0 \end{bmatrix} \tag{3}$$

The inputs u for this work were recorded from the Pixhawk autopilot that purposely was not connected to a GPS receiver. More details regarding the hardware configuration are provided in Section 5 below.

3.1 Measurement Updates

There are several measurement updates used in the developed EKF, they include a wind pseudo-measurement, a velocity update from the visual odometry, an altitude update from the baro altimeter, and finally the range measurement. The measurement models are described briefly below.

1) Wind Pseudo-Measurement: The wind pseudo-measurement update is the same proposed in [14], where the geometry in the wind triangle is used to equate the wind, ground and air speeds using the angles χ and ψ. This measurement is more of a constraint, as the ”measurement” should always equal zero.

$$h_w(x,u) = \begin{bmatrix} 0 \\ 0 \end{bmatrix} = \begin{bmatrix} V_a \cos(\psi) + \omega_n - V_g \cos(\chi) \\ V_a \sin(\psi) + \omega_e - V_g \sin(\chi) \end{bmatrix} \tag{4}$$

2) VO Velocity Update: The VO algorithm used is described in [15]. An important point about the algorithm is that yaw information, from a magnetometer, has been infused into the VO measurements. Consequently, the measurement provides both a ground speed and course angle update for the filter. A velocity update is used since the position information derived from the VO algorithm is relative to the image before it and does not provide position information relative to the navigation frame [16]. However, the VO algorithm is provided the best estimate of the rotation between the current body frame and the navigation frame, allowing it to express the velocity in the navigation frame. We can then update both the course angle x and the ground speed V_g elements of the state with the output of the VO velocity $[V_n, V_e, V_a]$ according to

$$z_{vo}(x) = \begin{bmatrix} \tan^{-1}\left(\frac{V_e}{V_n}\right) \\ \sqrt{V_n^2 + V_e^2 + V_a^2} \end{bmatrix} \tag{5}$$

Consequently, the measurement function is trivially,

$$h_{vo}(x) = \begin{bmatrix} \chi \\ V_g \end{bmatrix} \tag{6}$$

3) Altitude Update: The altitude update is simple, the information from the autopilot's barometer which directly updates the altitude state

$$h_a(x) = p_a \tag{7}$$

4) Ranging Update: The measurement of range between the lower vehicle and the upper vehicle includes the actual range in meters between the two vehicles, as well as the GPS coordinates in latitude, longitude, and height of the upper vehicle. We utilize a single GPS measurement of the lower vehicle, taken at the beginning of the flight, to define a common navigation frame of reference for both vehicles and to initialize the GNSS denied vehicle's position state. Thereafter we only use the lower vehicle GPS measurements for truth data. We do not address the issue of obtaining a common navigation reference frame between two vehicles for the case when GPS is never available for the lower vehicle; in such an instance, an estimate of the upper vehicle's position would likely need to be added to the filter state and a different coordinate system utilized. The measurement function used is

$$h_r(x, u_u) = \sqrt{(u_n - p_n)^2 + (u_e - p_e)^2 + (u_d + p_a)^2} \tag{8}$$

where $u_u = [u_n, u_e, u_d]^T$ are the coordinates of the upper vehicle in the now-common navigation frame. Recall that ud and pa point in opposite directions.

3.2 Filter Implementation

The above methods were implemented in the Scorpion Estimation Framework, created by the Autonomy and Navigation Technology Center (ANT) at the Air Force Institute of Technology. The implementation used an Extended Kalman Filter and the data was run post-process through the filter. All the results pertain to estimating the states of a lower UAV using the filter described.

4 OBSERVABILITY ANALYSIS

The observability rank condition for nonlinear systems outlined in Chapter 7 of [17], which is also summarized quite well in [18], pertains to the case where the nonlinear equations can be expressed linearly in the control:

$$\dot{x} = f(x) + \sum_{i=0}^{m} u_i(t) g[x(t)] \tag{9}$$

$$y_j = h_j(x), \text{ for } j = 1{:}\, l \tag{10}$$

Upon examining the models defined in Section 3 above, it is apparent that the filter model utilized does not exactly fit this constraint. The process to find the observability rank condition for such a system becomes much more arduous, involving many more uses of the chain rule. We have found that by neglecting second-order and higher derivatives with respect to u, whose magnitudes are usually small, the same result for the observability index may be achieved, namely

$$\mathcal{O} \approx \begin{bmatrix} \frac{\partial L_f^0 h_j(x,u)}{\partial x} \\ \frac{\partial L_f^1 h_j(x,u)}{\partial x} \\ \vdots \\ \frac{\partial L_f^i h_j(x,u)}{\partial x} \end{bmatrix} \tag{11}$$

with

$$L_f^0 h_j(x,u) = h_j(x,u)$$

$$L_f^{i+1} h_j(x,u) = \frac{\partial L_f^i h(x,u)}{\partial x} f(x,u)$$

Where the notation $L_f h_j(x,\ u)$ denotes the Lie derivative of the function $h_j(x,\ u)$ with respect to the vector field $f(x,\ u)$, which results in a scalar; and $i\ \epsilon\ n\ -\ 1$ and $j\ \in\ l$. A Lie derivative describes the information within the function $h_j(x,\ u)$ that is contained along the vector field $f(x,\ u)$. Then gradients of the Lie derivatives are used to assemble the observability index. The l = 6 measurement equations from Eqs.4, 6, 7, 8 form the set of $h_j(x,\ u)$ for the system. Note that assuming partial derivatives with respect to u are zero is actually a more conservative estimate than computing and including those terms.

4.1 Analytic Observability

The first step in assembling in (11) is to compute the gradient of the nonlinear measurement functions, (4), (6), (7), (8), with respect to the state x. For reference, h_1 and h_2 are from (4), h_3 and h_4 from (6), h_5 from (7) and h_6 from (8) respectively. This is found in (12) below.

$$\frac{\partial L_f^0 h_j(x,u)}{\partial x} = \begin{bmatrix} 0 & 0 & -\cos(\chi) & V_g\sin(\chi) & 1 & 0 & -V_a\sin(\psi) & 0 & 0 \\ 0 & 0 & -\sin(\chi) & -V_g\cos(\chi) & 1 & 0 & V_a\cos(\psi) & 0 & 0 \\ 0 & 0 & 0 & 1 & 0 & 0 & 0 & 0 & 0 \\ 0 & 0 & 1 & 0 & 0 & 0 & 0 & 1 & 0 \\ \frac{p_n-u_n}{\sqrt{\sigma_1}} & \frac{p_e-u_e}{\sqrt{\sigma_1}} & 0 & 0 & 0 & 0 & 0 & \frac{p_a+u_d}{\sqrt{\sigma_1}} & 0 \end{bmatrix} \quad (12)$$

where

$$\sigma_1 = (p_e - u_e)^2 + (p_n - u_n)^2 + (p_a + u_d)^2$$

Equation (12) provides the first 6 rows to (11); note that the boldfaced $h(x,\ u)$ implies that the partials for each $h_j(x,\ u)$ have been stacked to form a matrix. In (12) there is only one state, p_a, that does not receive any information from the measurements directly. However, the rank of (12) is only six, thus we require at least three more linearly independent equations in $\mathcal{O}$ to achieve local observability of the system.

The second row of (11) requests the partial of $L_f^1 h_j(x,u)$. Using the chain rule, this becomes

$$\frac{\partial L_f^1 h_j(x)}{\partial x} = \left(\frac{\partial^2 h_j(x)}{\partial x^2} f(x)\right)^T + \frac{\partial h_j(x)}{\partial x}\frac{\partial f(x)}{\partial x} \tag{13}$$

where $\frac{\partial^2 h_j(x)}{\partial x^2}$ is the Hessian of $h_j(x)$. It is useful to look at both of the terms in (13) to see what each part contributes to the observability.

The first half of (13) contains second-order derivatives and is quite sparse. Only measurement functions (4) and (8) contain non-zero terms. The second order gradients of these three measurements, multiplied by $f(x)^T$, results in three column vectors (14), (15), and (16) respectively.

$$\frac{\partial^2 h_1(x)}{\partial x^2} f(x) = \begin{bmatrix} 0 \\ 0 \\ \frac{g \sin(\chi)\tan(\varphi)\cos(\chi-\psi)}{V_g} \\ g\cos(\chi)\tan(\varphi)\cos(\chi-\psi) + \frac{V_a \sin(\chi)\psi\,(\omega_e \cos(\psi) - \omega_n \sin(\psi))}{V_g} \\ 0 \\ 0 \\ -V_a \cos(\psi)\psi \\ 0 \\ 0 \end{bmatrix} \tag{14}$$

$$\frac{\partial^2 h_2(x)}{\partial x^2} f(x) = \begin{bmatrix} 0 \\ 0 \\ \frac{g \cos(\chi)\tan(\varphi)\cos(\chi-\psi)}{V_g} \\ g\sin(\chi)\tan(\varphi)\cos(\chi-\psi) - \frac{V_a \cos(\chi)\sigma_2\,(\omega_e \cos(\psi) - \omega_n \sin(\psi))}{V_g} \\ 0 \\ 0 \\ -V_a \sin(\psi)\sigma_2 \\ 0 \\ 0 \end{bmatrix} \tag{15}$$

$$\frac{\partial^2 h_6(x)}{\partial x^2} f(x) = \begin{bmatrix} \frac{V_g \cos(\chi)}{2\sigma_1^{3/2}}(\quad_n + 2\sigma_1) + \frac{V_g \sin(\chi)}{\sigma_1^{3/2}} \quad_n + \Delta \quad) + \frac{\dot{p}_a}{\sigma_1^{3/2}} \quad_n - \Delta_d) \\ \frac{V_g \sin(\chi)}{2\sigma_1^{3/2}}(\quad_e + 2\sigma_1) + \frac{V_g \cos(\chi)}{\sigma_1^{3/2}} \quad_n + \Delta \quad) + \frac{\dot{p}_a}{\sigma_1^{3/2}} \quad_e - \Delta_d) \\ 0 \\ 0 \\ 0 \\ 0 \\ 0 \\ \frac{\dot{p}_a}{2\sigma_1^{3/2}}(2\sigma_1 - \Delta_d) + \frac{V_g \cos(\chi)}{\sigma_1^{3/2}}(\Delta_n - \Delta_d) + \frac{V_g \sin(\chi)}{\sigma_1^{3/2}}(\Delta_e - \Delta_d) \\ 0 \end{bmatrix} \tag{16}$$

where

$$\Delta_n = u_n - p_n$$
$$\Delta_e = u_e - p_e$$
$$\Delta_d = u_d + p_a$$

Equations (14), (15) and (16) are transposed and stacked, along with three zero row-vectors for measurement functions (6) and (7) to form the matrix representation of $\left(\frac{\partial^2 h(x)}{\partial x^2} f(x)\right)^T$, which is not shown due to size restrictions. Note the first two terms in (16) are non-zero. This information, though second-order, enables the observability of the horizontal position $[p_n,\ p_e]$. No second-order information contributes to the observability of $\dot{p}_n$.

The second half of (13) contains combinations of only first-order derivatives and is expressed in (17).

$$\frac{\partial h_j(x)}{\partial x}\frac{\partial f(x)}{\partial x} = \begin{bmatrix} 0 & 0 & \frac{V_a \cos(\chi)\sigma_1\sigma_2}{V_g^2} - \frac{g \sin(\chi)\tan(\varphi)\cos(\chi-\psi)}{V_g} & -\sigma_4 & \frac{V_a \cos(\chi)\sin(\psi)\dot{\psi}}{V_g} - \frac{V_a \cos(\chi)\cos(\psi)\dot{\psi}}{V_g}\sigma_4 + \frac{V_a \cos(\chi)\dot{\psi}\sigma_3}{V_g} & 0 & 0 \\ 0 & 0 & \frac{g \cos(\chi)\tan(\varphi)\cos(\chi-\psi)}{V} + \frac{V_a \sin(\chi)\dot{\psi}\ \sigma_2}{V_g^2} & \sigma_5 & \frac{V_a \sin(\chi)\sin(\psi)\dot{\psi}}{V_g} - \frac{V_a \cos(\psi)\cos(\chi)\dot{\psi}}{V_g} - \frac{V_a \sin(\chi)\dot{\psi}\sigma_3}{V_g}\sigma_5 & 0 & 0 \\ 0 & 0 & -\frac{g \tan(\varphi)\cos(\chi-\psi)}{V_g^2} & -\sigma_6 & 0 & 0 & 0 & 0 \\ 0 & 0 & -\frac{V_a \dot{\psi}\sigma_2}{V_g^2} & 0 & \frac{-V_a \sin(\psi)\dot{\psi}}{V_g} & \frac{V_a \cos(\psi)\dot{\psi}}{V_g} & -\frac{V_a \dot{\psi}\sigma_3}{V_g} & 0 & 1 \\ 0 & 0 & 0 & \frac{-V_g \Delta_e \cos(\chi)}{\sqrt{\sigma_1}} + \frac{V_g \Delta_n \sin(\chi)}{\sqrt{\sigma_1}} & 0 & 0 & 0 & 0 & \frac{2p_a + 2u_d}{\sqrt{\sigma_1}} \\ 0 & 0 & \frac{-\Delta_n \cos(\chi)}{\sqrt{\sigma_1}} - \frac{\Delta_e \sin(\chi)}{\sqrt{\sigma_1}} & & 0 & 0 & 0 & & \end{bmatrix} \tag{17}$$

where

$$\sigma_2 = \omega_e \cos(\psi) - \omega_n \sin(\psi)$$
$$\sigma_3 = \omega_n \cos(\psi) + \omega_e \sin(\psi)$$
$$\sigma_4 = g \sin(\chi - \psi) \sin(\chi) \tan(\varphi)$$
$$\sigma_5 = g \sin(\chi - \psi) \cos(\chi) \tan(\varphi)$$
$$\sigma_6 = \frac{g \sin(\chi - \psi) \tan(\varphi)}{V_g}$$

Equation (17) clearly adds observability information to $\dot{p}_a$, in the final column. However, there is not any additional information added for the horizontal position [p_n, p_e], marked by lack of non-zero terms in the first two columns.

Analytically, by combining the two parts of (13) with (12) we have a 12 by 9 matrix that is of rank 9. Meaning, we do not need any higher-order Lie derivatives to form (11). The reason that the observability matrix is of full rank with range to only one known landmark is that yaw information is provided to the filter through the visual odometry method we have chosen to use. Without the yaw information provided, the observability grammian would be of rank 8 and we would need at least one other known landmark to achieve full observability.

Interesting to note, however, is that if we were to follow a more conservative estimate of the observability and ignore any second-order and higher partial derivatives in (11), we would be left with multiples of (17), as shown in [17], with $\frac{\partial h^{(x)}}{\partial x} = C$ and $\frac{\partial f}{\partial x} = A$. (11) then can be expressed just as a linear system observability index

$$\mathcal{O}_l \approx \begin{bmatrix} C \\ CA \\ \vdots \\ CA^{n-1} \end{bmatrix} \tag{18}$$

Following this assumption, (11) would never be full rank and the system would not be observable, even though it should be. The only information available to the filter for horizontal position would be a nonlinear combination of p_n and p_e and it would not be separable. In Section 6, we analyze the rank and condition of the observability index (11) with the flight data for some additional insights in the observability question for this problem.

4.2 Average Normalized Estimation Error Squared

Another metric that proves useful in analyzing estimators is the Average Normalized Estimation Error Squared (ANEES) [19]. The ANEES metric shows insight into whether an estimator is credible by demonstrating and quantifying how much the results are optimistic or pessimistic. ANEES is defined as

$$\bar{\epsilon} = \frac{1}{M}\sum_{i=1}^{M}(x_i - \hat{x}_i)^T P_i^{-1}(x_i - \hat{x}_i) \tag{19}$$

where x is the true state, $\hat{x}$ is the estimated state, P is the covariance matrix and M is the number of timesteps.

If the ANEES of the filter is significantly greater than n (the length of x), the filter is optimistic; meaning that the covariance represented by the filter is too small. When the ANEES is significantly under n the filter is pessimistic and the covariance is too large. When an estimator is optimistic, it is overconfident in the estimate of the covariance bounds, which can lead to filter divergence.

5 FLIGHT TEST DETAILS

The data utilized in this research was collected from flight tests accomplished by AFIT in July 2017 at Himsel Field at Camp Atterbury, IN. Two Sig Rascal 110 model airplanes with 2.8 meter wingspans, driven by electric motors were flown. Data was collected onboard each plane and then brought together through post processing. Details regarding each plane are below.

5.1 Upper Plane

The upper plane was controlled using a Pixhawk autopilot in an autonomous loiter mode with a radius of 100 meters, at 18 meters per second, at an altitude of about 250 meters above the ground. The payload consisted of a small UDOO Quad computer and an ENSCO ranging radio. The computer logged data from the autopilot at about 4 Hz and Ranging data at about 20 Hz. A cubic spline interpolation method was used to up-convert the 4 Hz GPS coordinates to 20 Hz for processing at maximum ranging rates. The upper plane was launched first, followed by the lower plane.

5.2 Lower Plane

The lower plane was flown manually by a safety pilot on the ground. It was flown over an area directly below the upper plane but within a span of about 500 by 500 meters for about twelve minutes, at a speed of about 22 meters per second, within an altitude of between 75 and 150 meters.

The payload consisted of two Pixhawk autopilots (one disconnected from the GPS receiver), an ENSCO ranging radio, an Allied Vision Prosilica GT1290 camera, a five-point ethernet switch, and an Intel NUC computer. Data was logged onboard the NUC computer at variable rates, which proved a little challenging during post-processing: 9Hz monochrome camera images, 20Hz ranging data, 140Hz GPS-denied IMU and altimeter, 5Hz GPS-denied airspeed, 4Hz GPS data.

6 RESULTS

We begin by reviewing high-level results and then we will descend down into greater detail. First we will review the filter performance using the overall root-mean squared (RMS) error in North and East directions and examine what happens as we change the update rate for both VO data and Ranging data. Next we examine some approximated ANEES results for some of the filter states, which provides some insight into how consistent the filter is performing. We do not have truth data for all the filter states and some of this data had to be approximated, e.g. velocity information obtained through a numerical derivative with a low pass filter of the position data; nevertheless looking at ANEES provides insight into the performance of the filter. The state estimates are next examined in detail to get a better perspective on what the provided overall RMS and ANEES numbers really mean. Finally, we provide numerical results of the Observability Index (11).

6.1 RMS Results

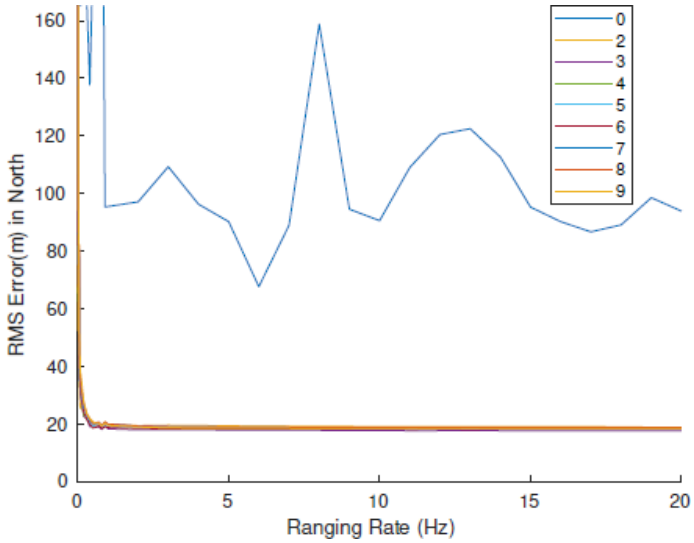

Figure 2. The overall RMS error is shown in the North direction for position, at different VO update rates (different lines), and for different Ranging update rates (along X axis). Notice how the RMS error drops dramatically with the introduction of range data. By about 3Hz or so, there is minimal improvement for faster range measurement update rates. Note the differences between not having VO data (0 line) and having range data (the other lines). The filter was largely tuned on 3Hz VO data.

The filter was run across a wide range of update rates for the VO and Ranging measurements and the overall RMS values were extracted for each run. The VO update rate was varied from 0 to 9 Hz, in integer steps. The Ranging was varied from 0 to 20 Hz in integer steps and then additionally at lower rates between 0 and 1Hz: 0.01Hz to 0.09Hz by 0.01Hz steps and 0.1Hz to 0.9Hz by 0.1Hz steps. Running the filter across this wide swath of measurement update rates allows visibility into trends in the data. Insight into how the filter performance varies with the VO and Ranging update rates is apparent.

We note that the filter was not tuned independently for each of these iterations and so is not optimal at all points shown. Tuning was completed using the first 300 seconds of data from the flight on a few selections of VO and Ranging update rates, predominately at 3 Hz VO and 4 Hz Ranging. Then, the entire batch at all ranging and VO update rates was computed using the same tuning parameters. Again, this approach is sub-optimal but makes the analysis feasible. The VO algorithm was not able to compute solutions over the entire flight for the 1 Hz and 2 Hz settings. The 1 Hz results are excluded, as the duration was only about 130 seconds. The 2 Hz so these results are still shown, but the data reach only 552 seconds into the flight, instead of the full 720. The lines for 0Hz in the figures below signify that VO information was not used, only internal autopilot sensors and range data. The datapoints at 0Hz Ranging correspond to cases where no range data was utilized, only internal sensors and VO measurements.

Figure 2 provides a glimpse of the overall RMS error in the north position of the lower plane. The lines in the figure correspond to different rates of VO measurements, noted by the legend. The x-axis refers to the Ranging measurement update rates. Note how quickly the RMS error drops at the beginning of the figure; it does not take a high rate of Ranging data to begin to bound the drift in the filter. This is shown more clearly in a zoomed-in version of Figure 2 in Figure 3.

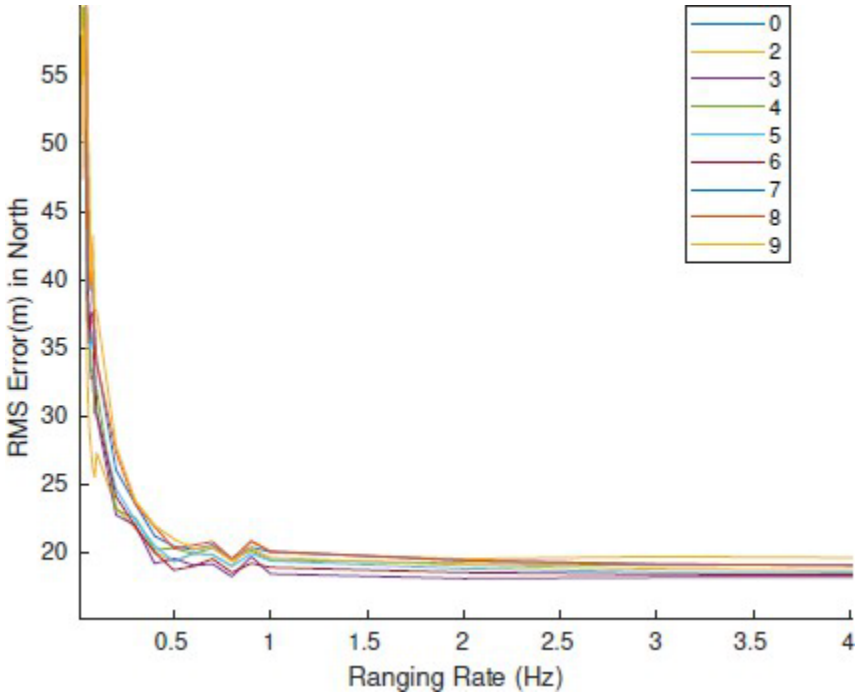

Figure 3. Zoomed version of Figure 2, showing the steep descent of RMS error with range rate. It was found that even Ranging data at 0.01 Hz (once every 100 seconds) was sufficient to bound the covariance of the filter. Also, for clarity, the line for 0 Hz VO was removed.

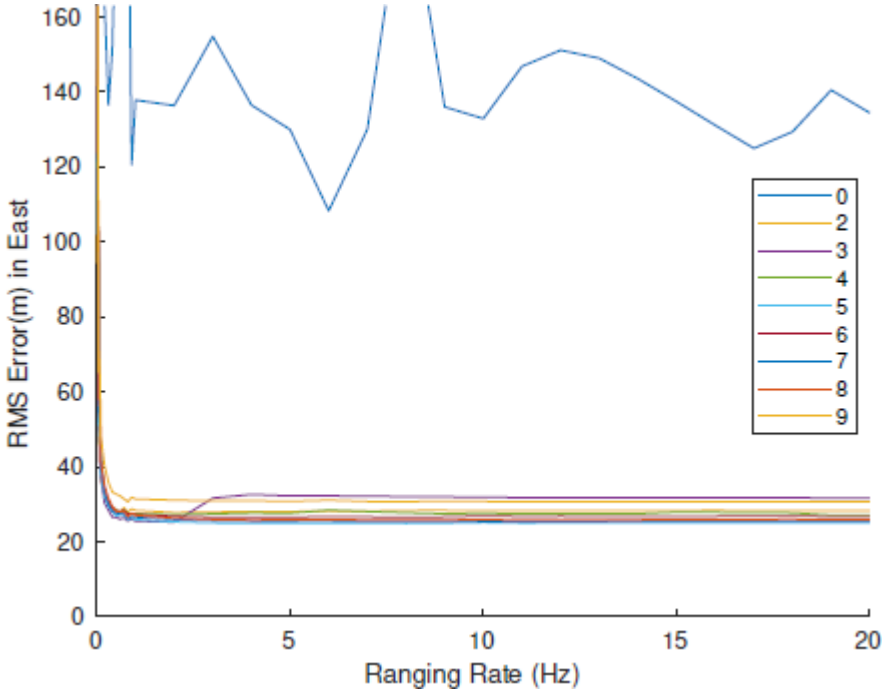

Figure 4. The overall RMS error in the East direction is shown, at different VO update rates (lines), and for different Ranging update rates (along x axis). Notice how the RMS error drops dramatically with the introduction of range data. By about 3Hz or so, there is minimal improvement for faster range measurement update rates. Note the differences between not having VO data (0 line) and having range data. The filter was largely tuned on 3Hz VO data.

By about 3Hz Ranging, there is minimal improvement by including Ranging data any faster. A similar story is found in examining the East RMS error in Figure 4 below.

Figures 2 and 4 also illustrate that there is a significant difference in the performance of the filter when VO data is removed, shown by the line labeled “0” and the performance with some VO data, all the remaining plot lines. This difference could be made more drastic by a state of the art VO algorithm; the algorithm utilized is a basic comparison of two images and does not do any advanced processing, such as tracking features over multiple frames or bundle adjustment. There is also some difference in performance among the different VO rates, but not by a large margin; 3Hz VO data is a better performer over many range rates in the two figures. Recall that tuning of the filter was completed using the first 300 seconds of data from the flight on a few selections of VO and Ranging update rates, predominately 3 Hz VO and 4 Hz Ranging. Then, the entire batch at all ranging and VO update rates was computed using the same tuning parameters. Consequently, the 3 Hz line represents a bounding of the performance of this VO system and any of the other VO update rates could be tuned down to close to this performance.

6.2 ANEES

Figure 5 displays the ANEES over the whole batch of VO and Ranging update rates. This computation of ANEES only considers the three position states in the filter p_n, p_e and p_a and the associated reduced covariance. The ANEES for all these lines should therefore be at 3 for all permutations of VO and Ranging updates. On the whole, the filter is inconsistent and the estimated covariance is smaller than the true covariance actually is, with the only exception being the 2 Hz VO results, which are slightly under-confident. However, this inconsistency is not egregious. Detailed state estimates will be shown in the next section, and as will be seen, there are only a few periods of the 12 minute flight that are responsible for the ANEES to be higher than it ought to be.

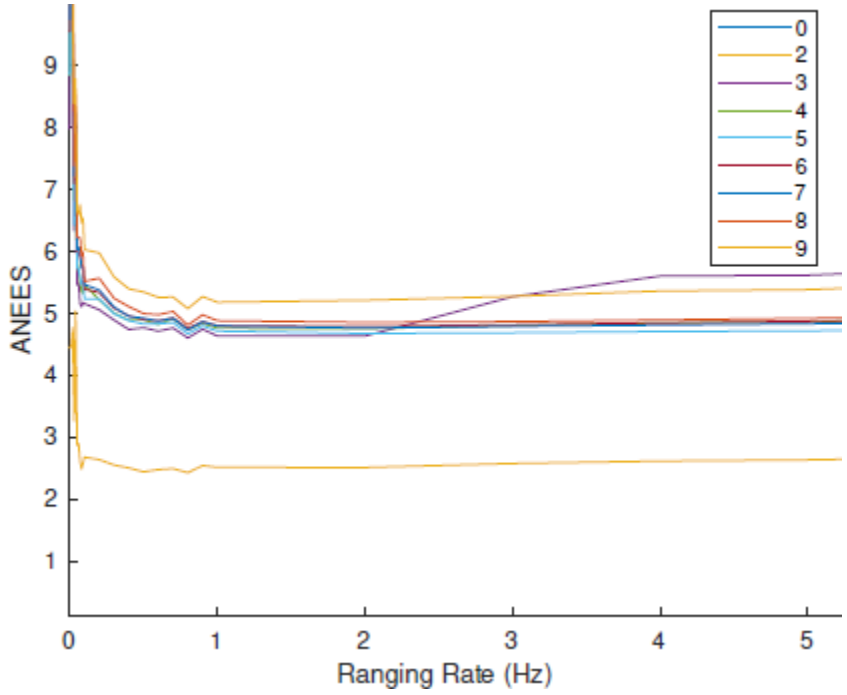

Figure 5. This figure shows the ANEES for only the 3D position data $[p_n, p_e, p_a]$, at different VO update rates (lines), and for different Ranging update rates (X axis). The line for 0Hz VO is not visible in this figure, as it was zoomed to show detail on the other lines. The ANEES for a consistent filter in this scenario would lie at 3, since there are three states considered in this calculation. Only the 2 Hz VO line is below 3, meaning that it is slightly under-confident (covariance is slightly bigger than it actually is).

6.3 Detailed State Estimates

Detailed results of the filter performance for the state estimates are discussed in this section. First we examine state error estimates for the case of 5 Hz VO and 3 Hz Ranging, one of the best cases shown in Figures 2 and 4. Next the filter results at 8 Hz VO and 0.2 Hz Ranging are shown to demonstrate the results with a slow Ranging update and middle of the road performance. Next a quick review of the position results at 4 Hz VO and 0.01 Hz Ranging are shown, demonstrating that bounding of the filter covariance occurs even at that low Ranging rate. The results for 0 Hz Ranging and then 0 Hz VO are then shown to demonstrate that the filter performs as expected at the extremes. Overall, the results will demonstrate a converging but slightly overconfident filter; and most importantly, a filter covariance that is bounded by the inclusion of Ranging information to one other vehicle with known pose.

1) 5 Hz VO and 3 Hz Ranging: Figure 6 shows the errors in the state estimates of the filter over the whole flight, with VO updates at 5 Hz and Ranging updates at 3 Hz. Also shown are 3σ bounds using the estimated covariance. Note that the filter covariances remain bounded over the trajectory even though Ranging data is available to only one landmark. As discussed in Section 4, the complete observability of the state is due to the combination of the yaw information provided by the VO algorithm and the range to the one known vehicle.
2) 8 Hz VO and 0.2 Hz Ranging: The errors in the states for a different scenario are presented in Figure 7. Here, VO data is received at 8 Hz and Ranging at 0.2 Hz. Similarities to the the case in Figure 6 can be seen, including similar locations in time where the filter estimates are not consistent. Note the larger scale of the y-axes in Figure 7. The 3σ bounds are larger and the performance in p_e is worse than before. The key point here is that the horizontal position is still bounded, even at the low rate of 0.2 Hz Ranging.
3) 0.01 Hz Ranging: Figure 8 demonstrates that the horizontal position is still bounded at the even lower rate of 0.01 Hz Ranging for 4 Hz VO; although the performance is quite worse than those with higher Ranging rates, as expected from Figure 2. This fact demonstrates that infrequent ranging data from a single known location is sufficient to bound the drift of a VIO estimation approach for fixed-wing UAVs that has access to yaw and pressure information.
4) Range-only Measurements: Figure 9 shows the error in the states when VO data is not available, but Ranging data is received at 10 Hz. Figure 9 demonstrates that the divergent-convergent cycle behavior exist even when VO data is not available. Note the drop in yaw (ψ) performance, which demonstrates that the χ update from the VO is providing the yaw information.
5) VO-only Measurements: Figure 10 plots the error in the state for 5 Hz VO and 0 Hz Ranging. As expected, the p_n and p_e estimates grow without bound since those positions are unobservable without the range. If the VO were not also providing yaw information through the χ measurement in (6), ψ would also be unobservable.

6.4 Numeric Observability

An evaluation of the numerical characteristics of the observability index can be completed by an inspection of the rank of the matrix (11) at all timesteps within the flight. If (11) is not full rank, the system is not observable.

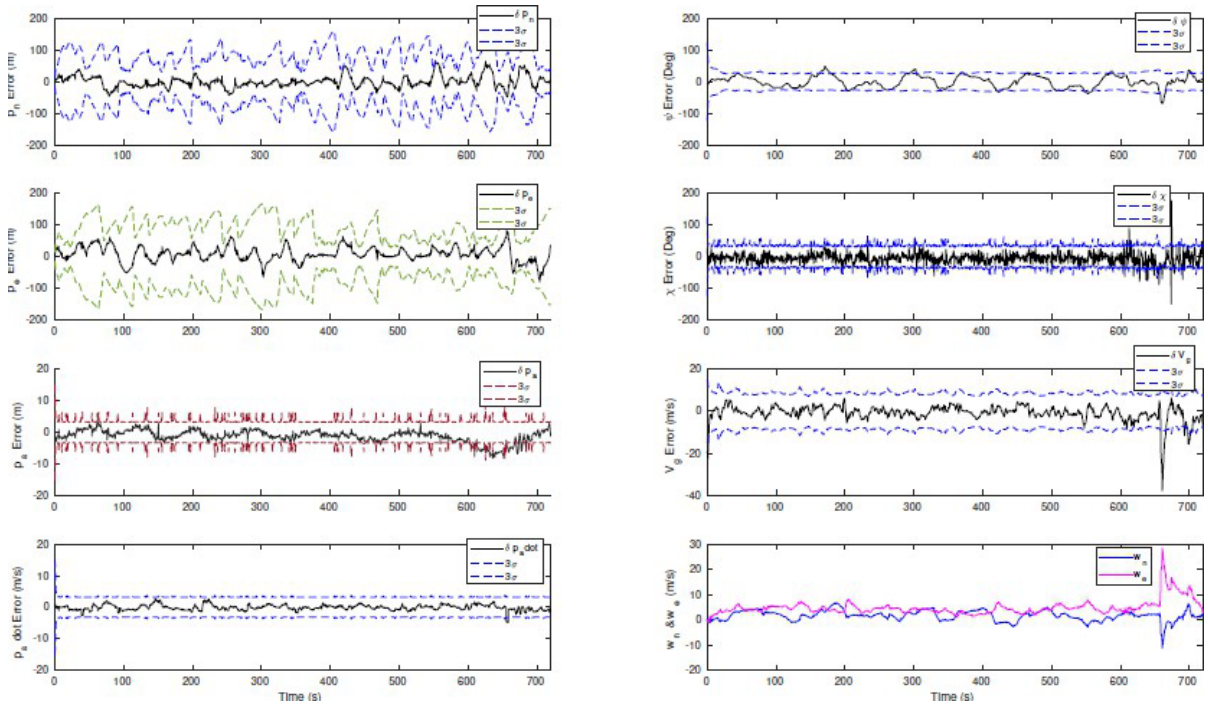

Figure 6. This figure displays the error in the states (except wind states - no truth information was available) along with 3σ bounds of the covariances for the scenario of 5 Hz VO and 3 Hz Ranging. For the most part, the states are well-behaved, meaning they remain bounded by the 3σ bounds, even though the accuracy is less than desirable. However, there are portions of the trajectory where errors in each state do exceed the bounds; ψ is particularly prone to overconfidence.

Figure 11 shows the rank of (11) evaluated using the filter states and inputs at about 4 Hz throughout the entire flight for the case of 5 Hz VO and 2 Hz Ranging. Note that it is full rank throughout the flight, as was expected from the analytic expression. Range to only one known landmark and the yaw information from the VO are sufficient to fully constrain the covariance of a VIO plus pressure system onboard a fixed-wing UAV. We note that the rank of was also full rank for every other combination of VO and Ranging update rates, with the exception of 0 Hz Ranging.

6.5 Condition Number

The problem with only analyzing the rank of (11) is that there is no additional information provided, no ability to see how strong the local observability condition is. The conjecture we pose, without proof as yet, is that if the observability index is poorly conditioned then the flow of information from the measurements to the states will be sensitive to errors and more fragile.

The condition number of a matrix gives an indication of the sensitivity of that matrix to changes in input for a computation like $Ax = b$. If the matrix A is poorly conditioned then small changes (or errors) in the input vector x can result in large changes (or errors) in the output vector b. The condition number is defined as a ratio of the largest to the smallest singular values of a matrix. Ideally, it should be equal, or close to, one for a well-conditioned matrix.

Recall that the observability index $\mathcal{O}$ represents how information from the measurements and the prediction model flows the states. If the rank of (11) is deficient it means that there is insufficient information from the measurements and model to distinguish the state at one time with the state at another time.

Analytically, (11) was shown to be full rank in Section 4. However, there are one or two segments of the flight where state estimates begin to diverge and then the filter quickly reconverges. This is clearly seen in the detailed state plots above as well as the attached video of the 3D plots.

Figure 12 plots the condition number of (11) over the whole flight, again for 3 Hz VO update rate and 1 Hz Ranging. The condition is quite poor for some periods of the flight.

Although a little difficult to see from Figure 12, the minimum condition number for this scenario is 303, the mean is 3.1e3 and the mode is 386. There are several times in the flight when the condition number reaches very high (greater than 6e4) and once were it ascends to over 2.2e5, clearly denoting that the system is approaching being unobservable from a numerical stability standpoint.

The condition number of (11) throughout the flight with different ranges and update rates are similar in nature, denoting that different rates of measurement are not affecting the quality of the observability of the system. To improve the condition number, and thus the observability of the system, more measurements are needed. This result is not surprising due to the expectations going into the program. Range to another landmark would provide this information, changing the condition of and improving the performance; however, it is important to realize that range to a single landmark can drastically improve system performance of a GPS-denied, visually guided UAV by bounding the drift in the planar position states.

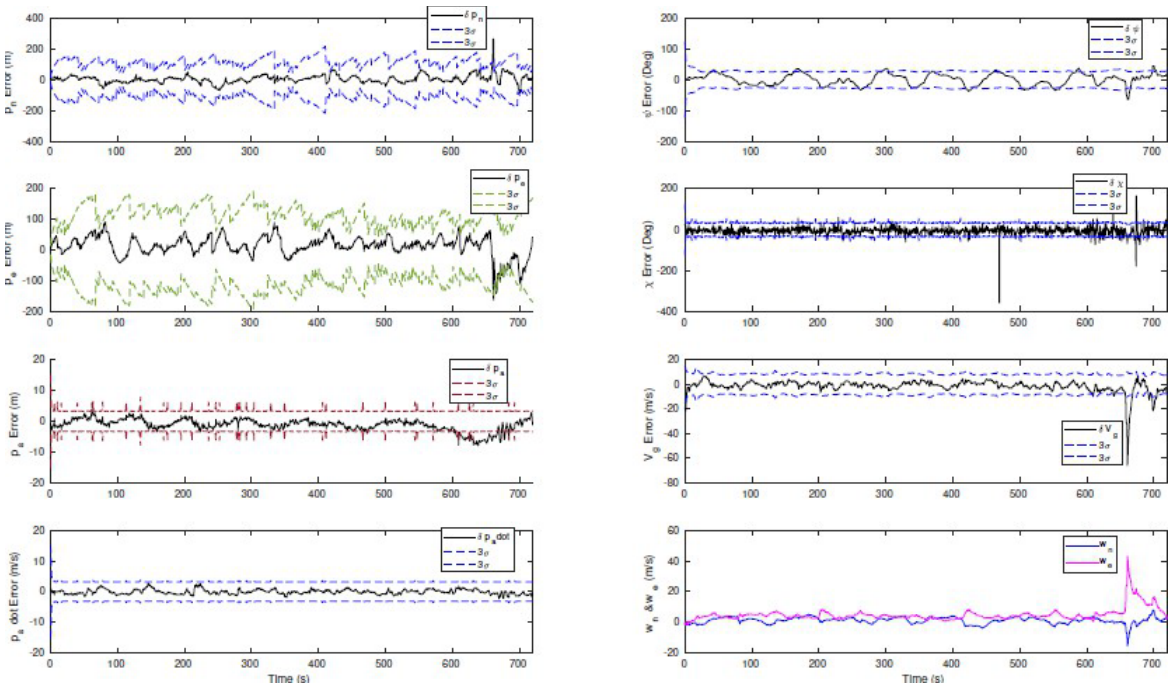

Figure 7. The error in the states are shown with the exception of wind states, where truth data was not available, along with 3σ bounds of the covariance for the scenario of 8 Hz VO and 0.2 Hz Ranging. The results are fairly similar to those in Figure 6 above. Note differences in the scales on the y-axes. The largest difference from the results in Figure 6 is the performance in p_e.

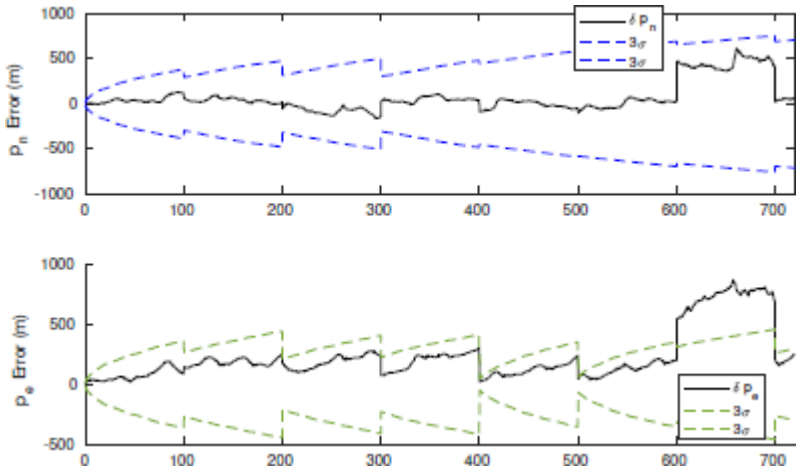

Figure 8. The error in the horizontal position states are shown along with 3σ bounds of the covariance for the scenario of 4 Hz VO and 0.01 Hz Ranging. The position covariance is bounded, even though ranging data is only received every 100 seconds.

7 CONCLUSIONS

A couple of conclusions can be drawn from the results demonstrated above. The first is that range to a single vehicle with known global position provides a tremendous benefit to a vehicle using a relative vision approach, like VO. The range information allows the vehicle to constrain the global drift and make the vision data begin to match up with the true trajectory, when pressure and magnetometer data are available. A key take-away is that even though the global position is observable in this scenario, the solution is poorly conditioned and can exhibit regions of divergence before the solution re-converges. It is possible that the solution at those points becomes multi-modal, with several positions being near-equally likely. Perhaps the use of a multi-modal filter, like a particle filter, would alleviate some of these issues. In the future we plan to investigate the use of a particle filter on this problem, through the Scorpion framework.

The second conclusion is a follow-on to the first. Ranging data is not needed at high rates to be effective at constraining global drift. It was observed that a rate of 0.01 Hz, or once every 100 seconds, was sufficient to bound the filter covariance over the 12 minute flight available for this data analysis. Granted, faster rates than 0.01 Hz do help with the accuracy of the solution, but the improvement is minimal above an update rate of about 3 Hz, for the scenario investigated. The benefit of this result is the ranging radio frequencies can be further utilized for other operations on the vehicle.

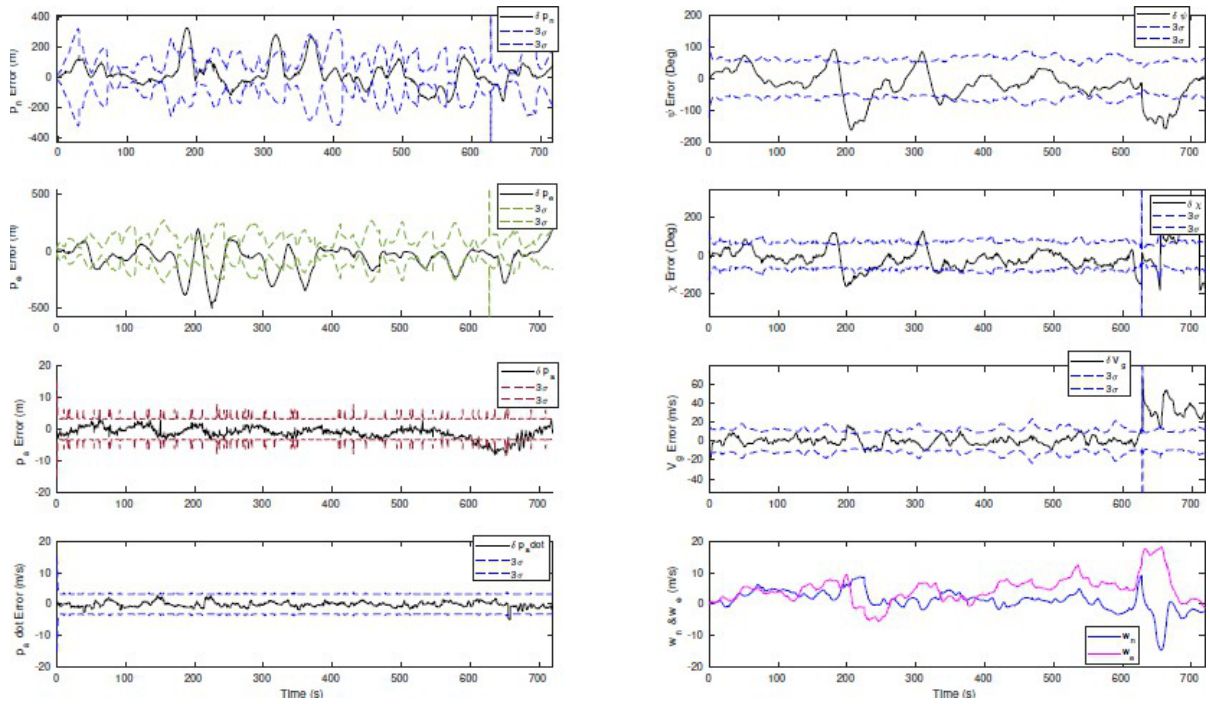

Figure 9. This figure displays the error in the states, again with exception of the wind states, along with 3σ bounds of the covariance for the scenario of 0 Hz VO and 10 Hz Ranging, in other words, VO data was not used for these results. Note differences in the scales on the y-axes.

8 ACKNOWLEDGMENT

We would like to thank Rick Patton and Dave Thacker for their help and expertise with the UAVs. We also acknowledge and are grateful for the previous work completed by Tim Machin and Ben Fain.

9 DISCLAIMER

The views expressed in this paper are those of the authors and do not reflect the official policy or position of the United States Air Force, Department of Defense, or U.S. Government.

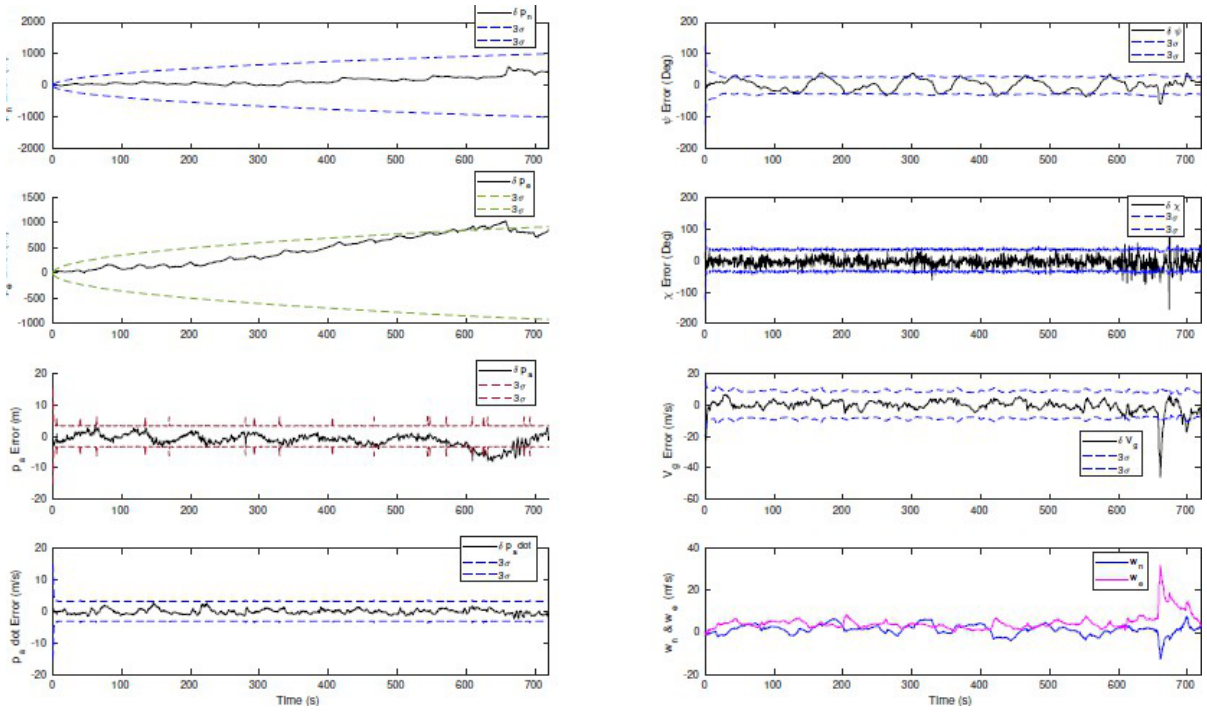

Figure 10. This figure displays the error in the states along with 3σ bounds of the covariance for the scenario of 5 Hz VO and 0 Hz Ranging, in other words, Ranging data was not used for these results. The horizontal position will grow without bound in this case, as those positions are unobservable without Ranging information.

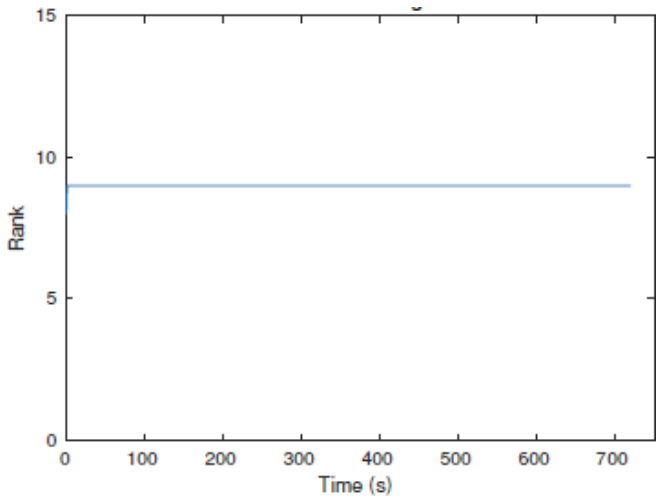

Figure 11. The rank of (11) for the case of 5 Hz VO and 2 Hz Ranging updates. Note that the matrix is full rank throughout the flight, $length(x) = 9$. The $\mathcal{O}$ matrix is also full rank for every other combination of VO and Ranging updates, with the exception of 0 Hz, or no Ranging information.

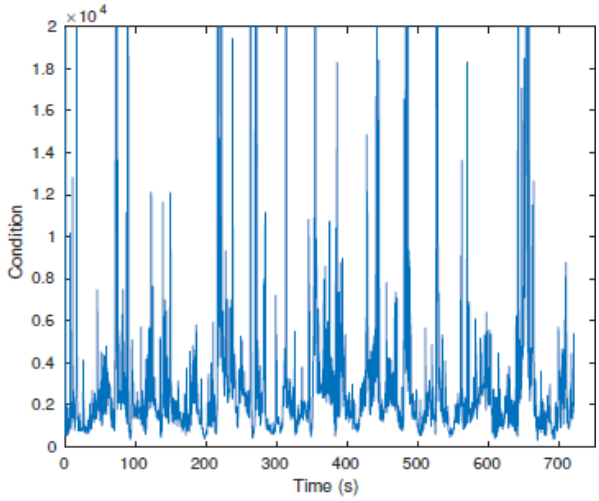

Figure 12. The condition number of (11) for the case of 5 Hz VO and 2 Hz Ranging updates, note the exponent applied to the y-axis. Even though the matrix is full rank throughout the flight, the matrix is poorly conditioned in several periods of the flight. It is not surprising, based on this result shown here, that there are portions of the trajectory where the filter begins to diverge and then reconverges.

10 REFERENCES

[1] Forster, L. Carlone, F. Dellaert, and D. Scaramuzza, “On-Manifold Preintegration for Real-Time Visual Inertial Odometry,” *IEEE Transactions on Robotics*, vol. 33, no. 1, pp. 1–21, 2017.

[2] Sa, M. Kamel, M. Burri, M. Bloesch, R. Khanna, M. Popovic, J. Nieto, and R. Siegwart, “Build your own visual-inertial odometry aided cost-effective and open-source autonomous drone,” *submitted to IEEE RAM*, pp. 1–21, 2017. [Online]. Available: http://arxiv.org/abs/1708.06652

[3] Y. Lin, F. Gao, T. Qin, W. Gao, T. Liu, W. Wu, Z. Yang, and S. Shen, “Autonomous aerial navigation using monocular visual-inertial fusion,” *Journal of Field Robotics*, no. May, pp. n/a–n/a, 2017. [Online]. Available: http://dx.doi.org/10.1002/rob.21732

[4] H. Bai and C. N. Taylor, “Control-enabled Observability in Visual-Inertial Odometry,” in *International Conference on Unmanned Aircraft Systems (ICUAS)*, Miami, FL, 2017.

[5] Y. Ling, T. Liu, and S. Shen, “Aggressive quadrotor flight using dense visual-inertial fusion,” in *Proceedings - IEEE International Conference on Robotics and Automation*, vol. 2016-June, 2016.

[6] M. Bloesch, S. Omari, M. Hutter, and R. Siegwart, “Robust visual inertial odometry using a direct EKF-based approach,” *IEEE International Conference on Intelligent Robots and Systems*, vol. 2015-Decem, pp. 298–304, 2015.

[7] V. Sazdovski, A. Kitanov, and I. Petrovic, “Implicit observation model for vision aided inertial navigation of aerial vehicles using single camera vector observations,” *Aerospace Science and Technology*, vol. 40, pp. 33–46, 2015. [Online]. Available: http://dx.doi.org/10.1016/j.ast.2014.09.019

[8] J. Engel, J. Sturm, and D. Cremers, “Scale-aware navigation of a low-cost quadrocopter with a monocular camera,” *Robotics and Autonomous Systems*, vol. 62, no. 11, pp. 1646–1656, 2014. [Online]. Available: http://dx.doi.org/10.1016/j.robot.2014.03.012

[9] Forster, M. Pizzoli, and D. Scaramuzza, “Appearance-based Active, Monocular, Dense Reconstruction for Micro Aerial Vehicles,” *Robotics: Science and Systems X*, no. 200021, 2014.

[10] D. Scaramuzza and F. Fraundorfer, “Visual Odometry Part I: The First 30 Years and Fundamentals,” *Robotics and Automation Magazine*, no. December, pp. 80–92, 2011.

[11] Fraundorfer and D. Scaramuzza, “Visual odometry Part 2: Matching, Robustness, Optimization, and Applications,” *Robotics and Automation Magazine*, no. June, pp. 78–90, 2012.

[12] B. M. Fain, “Small Fixed-wing Aerial Positioning using Inter-vehicle Ranging Combined with Visual Odometry,” Ph.D. dissertation, Air Force Institute of Technology, 2017.

[13] H. Titterton and J. L. Weston, *Strapdown Inertial Navigation Technology*, 2nd ed. The Institution of Engineering and Technology, 2004.

[14] R. W. Beard and T. W. McLain, *Small Unmanned Aircraft*. Princeton University Press, 2012.

[15] J. Carson, J. F. Raquet, and K. J. Kauffman, “Aerial Visual-Inertial Odometry Performance Evaluation,” in *ION Pacific PNT*. Honolulu: Institute of Navigation, 2016.

[16] R. C. Leishman, J. Gray, and J. Raquet, “Utilization of UAV Autopilots in Vision-based Alternative Navigation,” in *GNSS+*. Portland, OR: Institute of Navigation, 2017.

[17] M. Vidyasagar, *Nonlinear Systems Analysis*, 2nd ed. Philadelphia, PA: Society for Industrial and Applied Mathematics, 2002.

[18] Y. Kawano and T. Ohtsuka, *Observability analysis of nonlinear systems using pseudo-linear transformation*. IFAC, 2013, vol. 9, no. PART 1. [Online]. Available: http://dx.doi.org/10.3182/20130904-3-FR-2041.00100

[19] X. R. Li, Z. Zhao, and V. P. Jilkov, “Practical measures and test for credibility of an estimator,” *Proc. Workshop on Estimation, Tracking, and . . .* , pp. 481–495, 2001.